

Replicating the Defect Structures on Ultrathin Rh Nanowires with Pt to Achieve Superior Electrocatalytic Activity toward Ethanol Oxidation

Kai Liu, Wei Wang, Penghui Guo, Jinyu Ye, Yuanyuan Wang, Pingting Li, Zixi Lyu, Yongsheng Geng, Maochang Liu, and Shuifen Xie*

Metal nanostructures with an ultrathin Pt skin and abundant surface defects are attractive for electrocatalytic applications owing to the increased utilization efficiency of Pt atoms and the presence of highly reactive sites. This paper reports a conformal, layer-by-layer deposition of Pt atoms on defective Rh nanowires for the faithful replication of surface defects (i.e., grain boundaries) on the Rh nanowires. The thickness of the Pt shell can be controlled from one monolayer up to 5.3 atomic layers. This series of Rh@Pt_{nL} ($n = 1-5.3$) core–sheath nanowires show greatly enhanced activity and durability in catalyzing the ethanol oxidation reaction in an acidic medium. Among others, the Rh@Pt_{3.5L} nanowires show the greatest mass activity (809 mA mg⁻¹_{Pt}) and specific activity (1.18 mA cm⁻²) after loaded on carbon support, which are 3.7 and 3.4 times those of the commercial Pt/C, respectively. In situ Fourier transform infrared spectroscopy studies indicate an enhanced interaction between the outermost Pt layer and the Rh nanowire can promote C–C bond cleavage for complete oxidation of ethanol to CO₂ while depress the dehydrogenation of ethanol to acetic acid. As the Pt shell thickness is increased, the selectivity for the CO₂ pathway decreases while that for acetic acid is increased.

1. Introduction

Electrocatalytic energy conversions are critical processes for facilitating the commercially widespread application of proton exchange membrane fuel cells (PEMFCs). Intensive fundamental works have been devoted to the design of efficient and durable electrocatalysts.^[1–5] To date, nanostructured Pt-based materials are admitted as the most effective electrocatalysts for accelerating both the anode and cathode reactions of fuel cells in acidic mediums.^[6–8] However, unsolved issues, including side reactions, sluggish reaction kinetics, intermedium poisons, instabilities, etc., still need to be addressed urgently through synthetic control of the Pt-based nanocatalysts.^[9–13] In particular, ethanol offers a superior fuel source for PEMFCs, due to its higher energy density (8 kWh kg⁻¹), lower toxicity, and reproducibility from biomass, etc. However, in the process of ethanol oxidation reaction (EOR), commonly, three different products, that is, acetaldehyde (CH₃CHO),

acetic acid (CH₃COOH), and CO₂, were obtained on Pt catalysts releasing 2, 4, and 12 electrons, respectively.^[14–17] The difficulty in C–C bond cleavage results in an incomplete oxidation of ethanol. To date, the efficiency of direct ethanol fuel cells (DEFCs) is restricted by the lack of active anode materials which can efficiently catalyze the C–C bond cleavage accomplishing ethanol complete oxidation to CO₂.

It has been universally recognized that the catalytic behavior of metal nanocrystals is highly dependent on their surface compositions and structures.^[18–20] Metallic nanocrystals with ultrathin Pt skins exhibit extraordinary electronic structures which can drastically improve their electrocatalytic performance.^[21–23] For example, dealloyed core–sheath metal nanocrystals, such as PtCu@Pt core–sheath nanocrystals and PtPb@Pt core–sheath nanoplates, were demonstrated to have extremely high activity and endurance for catalyzing the oxygen reduction reaction (ORR) owing to the geometric lattice strains and electronic ligand effects.^[24,25] On the other hand, metal nanocrystals with high density of surface defects are superior candidates for highly active electrocatalysts because the defect sites can act as reactive

K. Liu, W. Wang, Y. Wang, P. Li, Z. Lyu, Y. Geng, Prof. S. Xie
College of Materials Science and Engineering
Huaqiao University
Xiamen 361021, P. R. China
E-mail: sfxie@hqu.edu.cn

W. Wang, Prof. S. Xie
Shenzhen Research Institute of Xiamen University
Shenzhen 518000, P. R. China

P. Guo, Prof. M. Liu
International Research Center for Renewable Energy
State Key Laboratory of Multiphase Flow in Power Engineering
Xi'an Jiaotong University
Xi'an, Shaanxi 710049, P. R. China

Dr. J. Ye
State Key Laboratory of Physical Chemistry of Solid Surfaces
Department of Chemistry
College of Chemistry and Chemical Engineering
Xiamen University
Xiamen 361005, P. R. China

 The ORCID identification number(s) for the author(s) of this article can be found under <https://doi.org/10.1002/adfm.201806300>.

DOI: 10.1002/adfm.201806300

hot spots.^[26–29] As a model study, the electrocatalytic activities for formic acid oxidation catalyzed on twinned Pd nanocrystals that enclosed with the identical crystal facets were demonstrated to be gradually enhanced as the increasing of surface twin defect number.^[28] Based on above progresses, it is reasonable to deduce that conformal coating of an ultrathin Pt skin with optimized thickness on a second metal nanoseed equipped with high-density surface defects, to faithfully replicate the active defect sites out on the Pt shells as well as engender appreciable geometric lattice strain and electronic ligand effects, could offer a feasible strategy toward highly active electrocatalysts.

Ultrathin metal wavy nanowires (NWs), which are generated from an oriented attachment process and thus possess rich grain boundaries (GBs),^[30,31] can serve as typical highly defective nanocores for coating Pt skins. Herein, we demonstrate a facile route for conformally layer-by-layer coating of Pt atoms on the surface of defective Rh wave NWs to fabricate shell thickness controlled Rh@Pt_{nL} core–sheath NWs. The high-density surface GBs on the inner Rh NW were faithfully replicated out on the surface of the Pt sheath. Moreover, the thicknesses of the Pt sheaths can be precisely controlled from one atomic monolayer (1L) up to 5.3 atomic layers (5.3L). These defective Rh@Pt_{nL} core–sheath NWs were applied to catalyze EOR for

the application of DEFCs. Compared to the state-of-the-art Pt/C catalyst, the carbon-supported Rh@Pt_{nL} NWs exhibited great enhancements in both the current density and durability, owing to the integration of the active defect sites and the modulated geometric lattice strains and electronic ligand effects. Electrochemical in situ Fourier transform infrared (FTIR) spectroscopy indicated that the two pathways for the generation of CO₂ and acetic acid were fluctuant and closely correlated to the atomic layer numbers of the Pt shells on these core–sheath NWs.

2. Results and Discussion

Ultrathin Rh wavy NWs with a diameter around 1.9 nm and high-density GBs were initially synthesized in high yield according to a previous report (Figure S1, Supporting Information).^[27] Later, Pt atomic layers were conformally coated on the Rh NWs in an ethylene glycol (EG) solution using H₂PtCl₆·6H₂O as a Pt source. In order to regulate the atomic layer numbers of the outer Pt shell, different amounts of H₂PtCl₆·6H₂O were added during the coating process (see the Experimental Section in the Supporting Information). Figure 1a schematically shows the conformal, layer-by-layer

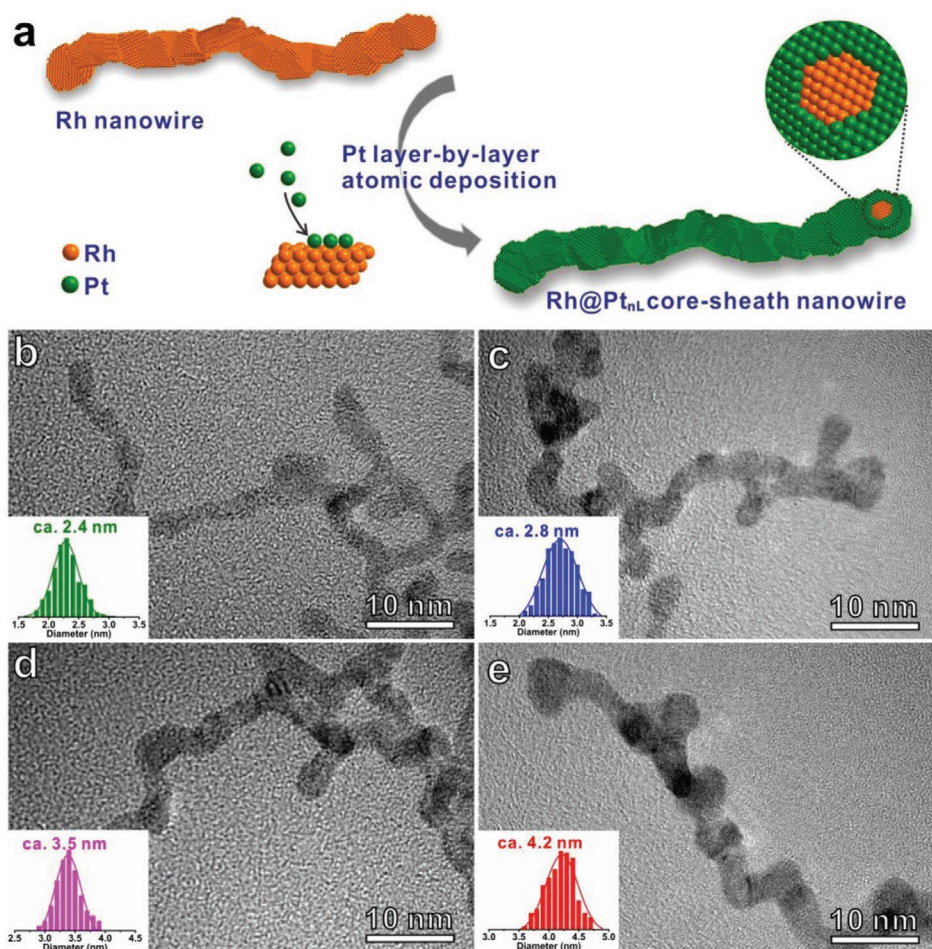


Figure 1. a) Schematic illustrating the conformal, layer-by-layer deposition of Pt atoms on ultrathin, wavy NWs of Rh. b–e) TEM images and diameter distributions of the Rh@Pt_{nL} core–sheath NWs: Rh@Pt_{1L}, Rh@Pt_{2L}, Rh@Pt_{3.5L}, and Rh@Pt_{5.3L}.

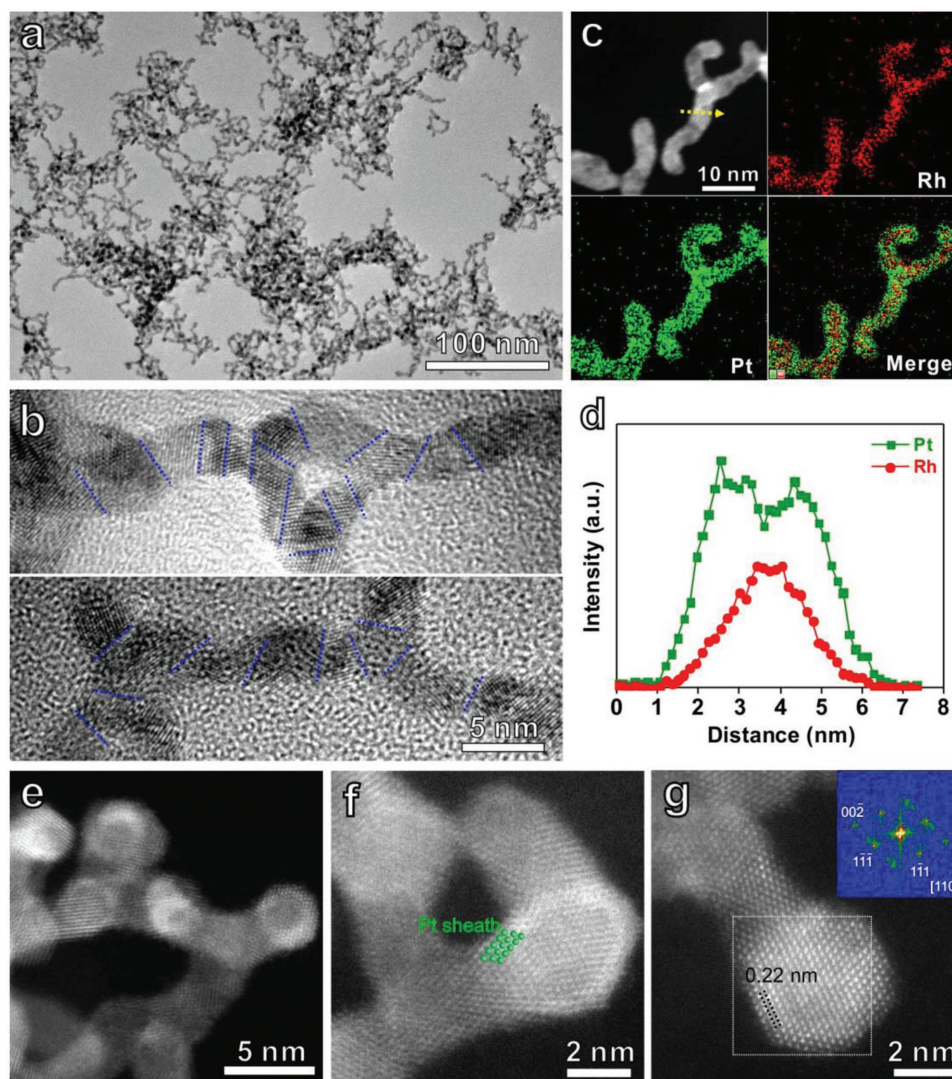


Figure 2. Structural characterizations of the as-prepared Rh@Pt_{3.5L} core-sheath NWs: a) TEM; b) HRTEM (with the blue dashed lines marking the domain boundaries along the NWs); c) STEM and the corresponding EDS elemental mapping; d) EDS line scan along the yellow arrow marked in (c); e–g) HAADF-STEM showing the bright, outer Pt sheaths. The inset in (g) shows the corresponding FFT pattern of the dashed square region.

coating of Pt atoms on the defective Rh NWs for fabricating the Rh@Pt_{nL} core-sheath NWs. The transmission electron microscope (TEM) images show that the coated products all well reserved the wavy NW structure (Figure 1b–e and Figure S2, Supporting Information), indicating the success of conformal coating. Statistically, the mean diameters for these Rh@Pt_{nL} core-sheath NWs were thickened from 1.9 to 2.4, 2.8, 3.5, and 4.2 nm, respectively. Assuming the wavy NWs are dominated by {111} facets,^[27,31] the atomic layer numbers of the Pt sheath can be calculated to be about 1L, 2L, 3.5L, and 5.3L, respectively. Corresponding X-ray diffraction (XRD) patterns only show a single pure face-centered cubic (fcc) phase for these Rh@Pt_{nL} core-sheath NWs (Figure S3, Supporting Information), because of the broadening of the diffraction peaks and the small deviations in peak positions between Rh and Pt. As the increase of the diameter of the Rh@Pt_{nL} core-sheath NWs, the positions of the (111) diffraction peaks were gradually shifted from the Rh phase close to the Pt phase, indicating the Pt fractions in the

core-sheath products are increased. Gradually increased Pt/Rh molar ratios were also confirmed by the energy-dispersive X-ray spectroscopy (EDS) and inductively coupled plasma mass spectrometry (ICP-MS) (Table S1, Supporting Information).

The structure and composition distribution of Rh@Pt_{3.5L} NWs were detailedly analyzed to visually illuminate the core-sheath structure of the Pt coated NWs (Figure 2). The low-magnification TEM image reveals the high yield production of the wavy NWs after coating (Figure 2a). The blue dashed lines in the high-resolution TEM (HRTEM) images evidently highlight the high density of defect sites cross-sectioning the Rh@Pt_{3.5L} core-sheath NWs (Figure 2b and Figure S4, Supporting Information). Figure 2c,d shows a scanning TEM (STEM) image of an individual Rh@Pt_{3.5L} core-sheath NW and the corresponding EDS composition mapping and cross-sectioning line scan. An enrichment of Rh at the central region (red) and the presence of an outer Pt shell (green) can be distinctly observed, verifying the segregated Rh@Pt core-sheath

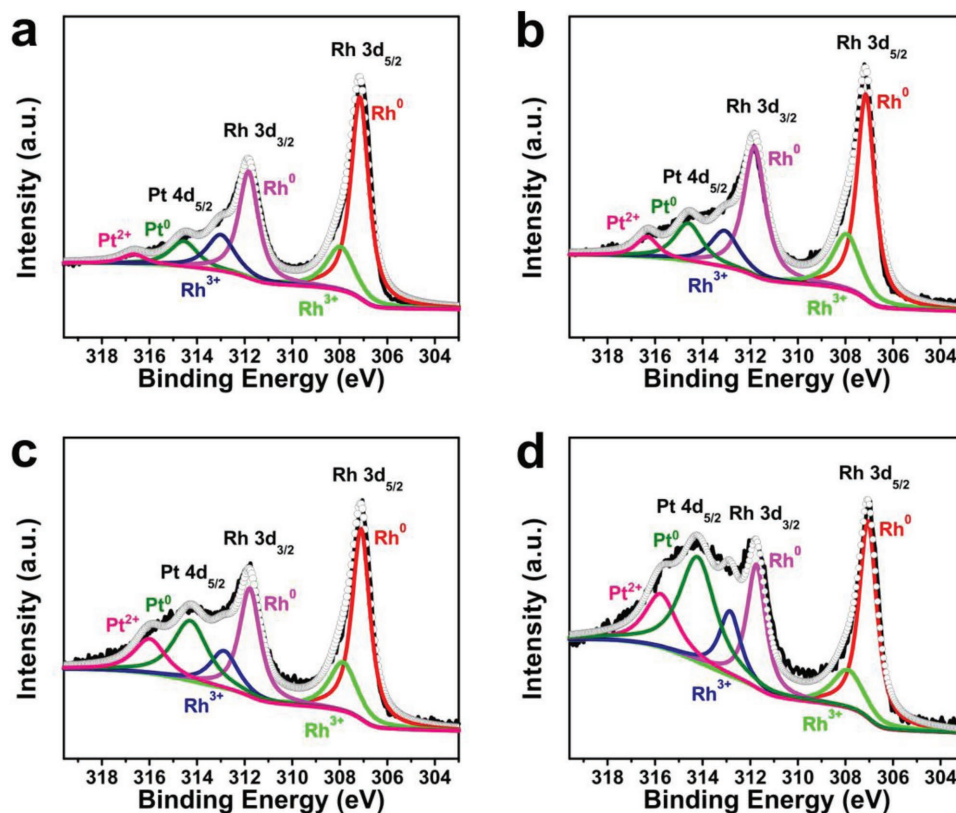


Figure 3. a–d) Analysis of the Rh 3d and Pt 4d XPS spectra recorded from the as-prepared Rh@Pt_{nL} core–sheath NWs: Rh@Pt_{1L}, Rh@Pt_{2L}, Rh@Pt_{3.5L}, and Rh@Pt_{5.3L}.

structure. The core–sheath structure can be further illuminated through high-angle annular dark-field STEM (HAADF-STEM) images due to the brighter Z-contrast of Pt atoms than that of Rh (Figure 2e,f). The *d*-spacing between lattice planes that paralleled to the surface of the NWs was 0.22 nm, indicating the major surface of the core–sheath Rh@Pt_{3.5L} core–sheath NWs were indeed enclosed by {111} facets, which can also be revealed by the corresponding fast Fourier transform (FFT) pattern (Figure 2g).

The surface defect structures of the Rh@Pt_{nL} core–sheath NWs were further intentionally inspected. As shown by the TEM images (Figures S2 and S5, Supporting Information), all the Rh@Pt_{nL} core–sheath NWs maintained extremely twisty together with the presence of high-density GBs. The corresponding statistic densities of GBs on the Rh NWs and the Rh@Pt_{nL} core–sheath NWs (Figure S6, Supporting Information) indicate only slight decline can be found on the samples with thicker Pt coating (i.e., Rh@Pt_{3.5L} and Rh@Pt_{5.3L} NWs). To further evaluate the surface defect and electronic characteristics, X-ray photoelectron spectroscopy (XPS) was applied to character the surface chemical states of these Rh@Pt_{nL} core–sheath NWs. As shown in Figure 3, the intensities of the Pt 4d referred to that of Rh 3d were gradually elevated as the increase of Pt atomic layer numbers. Each individual peak assigned to the Rh 3d or Pt 4d can be further split into two doublets, associated with Rh⁰/Rh³⁺ and Pt⁰/Pt²⁺, respectively. It has been indicated that the structural defects could serve as possible channels for oxygen incorporation.^[32] The Rh³⁺ and Pt²⁺ chemical states can

be assigned to the oxidized species, which have been approved to be favorably formed at the surface defect sites and increased with the density of the surface defects.^[27,33,34] Only little decline of the Pt²⁺ fraction was observed from both the Pt 3d and Pt 4f spectra with the thickening of Pt sheaths (Figure 3, Figure S7 and Table S2, Supporting Information), implying the density of GBs was no distinctly decreased after the Pt coating. It is also worth to mention that the binding energy (BE) of the Pt⁰ 4f on the Rh@Pt_{1L} NWs positively shifted by 0.12 eV compared to that of standard Pt. It was previously observed that the positive shift of Pt⁰ 4f could weaken the surface Pt–CO interaction.^[35,36] This upshifting was gradually faded as the increase of Pt atomic layer numbers (Table S2, Supporting Information), indicating the electronic ligand effects on the outermost Pt layer was weakened as the increase of the Pt shell thickness. Meanwhile, considerable compression strain is caused on the outer Pt shells due to the lattice mismatch between Rh and Pt (3.1%),^[37] which can also be released as the increase of the Pt atomic layer numbers.

It has been demonstrated that incorporation of Rh into Pt forming alloys can efficiently improve the electrocatalytic activity toward EOR as Rh has an infusive effect in promoting the C–C bond cleavage on PtRh bimetallic nanocrystals.^[38–40] The electrocatalytic activity of the Rh@Pt_{nL} core–sheath NWs for EOR in an acidic medium was evaluated in order to correlate the Pt atomic layer number with the electrocatalytic EOR polarization behavior. Before the electrocatalytic measurements, Rh@Pt_{nL} core–sheath NWs were loaded on carbon

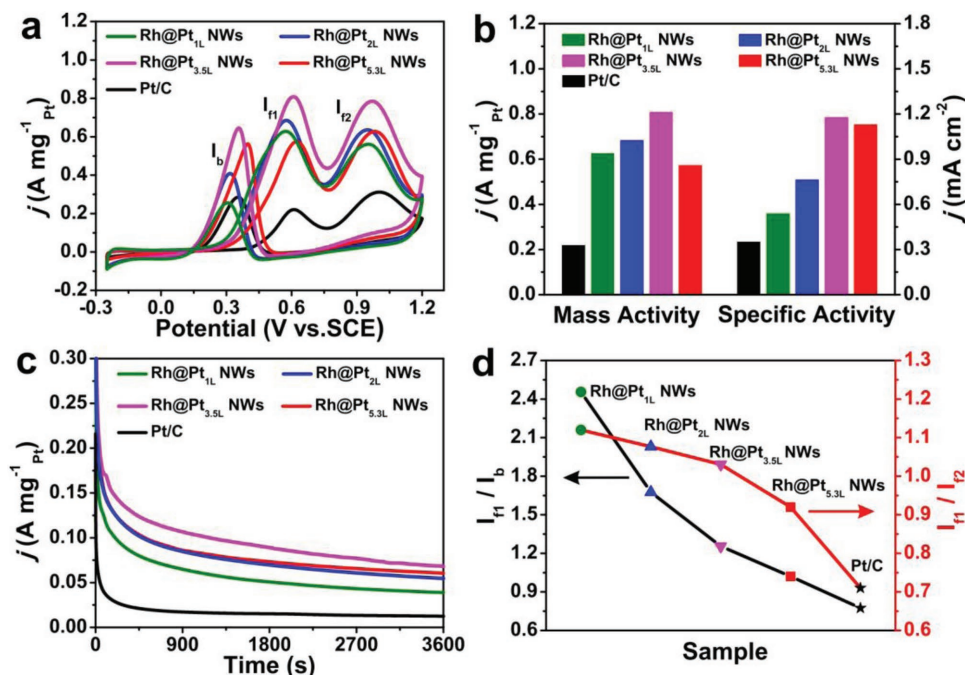


Figure 4. a) CV curves normalized to the Pt mass and b) histogram of the corresponding mass activities and specific activities of the Rh@Pt_{nL} NW/C and commercial Pt/C catalysts for EOR in 0.2 M ethanol and 0.1 M HClO₄ at 50 mV s⁻¹. c) Chronoamperometry measurements (*i*-*t*) of EOR recorded at 0.64 V (vs SCE) with the Rh@Pt_{nL} NW/C and commercial Pt/C catalysts at room temperature in 0.2 M ethanol and 0.1 M HClO₄. d) The values of *I*_{f1}/*I*_b and *I*_{f1}/*I*_{f2} derived from the EOR CV curves.

support (Vulcan XC-72, 25 wt% total metals, Figure S8, Supporting Information). The commercial Pt/C (JM, 20%, Figure S9, Supporting Information) was used as a benchmark catalyst for the comparisons. The electrochemically active surface areas (ECSAs) of all the catalysts were estimated by cyclic voltammetry (CV) in 0.1 M HClO₄. By calculating the charge transfer during the hydrogen adsorption/desorption (Figure S10, Supporting Information), the ECSA of Rh@Pt_{1L} NW/C, Rh@Pt_{2L} NW/C, Rh@Pt_{3.5L} NW/C, Rh@Pt_{5.3L} NW/C, and commercial Pt/C is determined to be 38.7, 42.0, 44.6, 39.2, and 56.0 m² g⁻¹, respectively.

We evaluated the EOR activity of the Rh@Pt_{nL} NW/C catalysts in 0.1 M HClO₄ and 0.2 M ethanol at 50 mV s⁻¹. Figure 4a and Figure S11 (Supporting Information) show the ethanol electrooxidation curves of different electrocatalysts with the current density normalized to the Pt mass and the ECSA, respectively. The Rh wavy NWs are inactive for EOR (Figure S12, Supporting Information), because Rh has much less capacity for dehydrogenation than Pt.^[41] Therefore, the activities for ethanol electrooxidation on these Rh@Pt_{nL} NW/C catalysts are completely stemmed from the outer Pt shells. At the forward scanning, ethanol electrooxidation gives two peaks, the first peak (peak f1) is commonly ascribed to the formation of acetaldehyde, acetic acid, and CO₂, whereas the second peak (peak f2) is almost completely attributed to acetic acid.^[39,42] The current density of peak f1 is commonly used to evaluate the activities of diverse electrocatalysts for EOR.^[16,43–47] Figure 4b shows a histogram of both the mass activity and specific activity in terms of peak f1 on these catalysts. As shown, the carbon-loaded Rh@Pt_{1L}, Rh@Pt_{2L}, Rh@Pt_{3.5L}, and Rh@Pt_{5.3L} NW/C catalysts exhibit 628 mA mg⁻¹_{Pt}, 685 mA mg⁻¹_{Pt}, 809 mA mg⁻¹_{Pt} and

574 mA mg⁻¹_{Pt}, respectively, which are all more active than the commercial Pt/C catalysts (221 mA mg⁻¹_{Pt}). For specific activity, as the Pt atomic layer numbers increased, the Rh@Pt_{nL} NW/C gave 0.54, 0.77, 1.18, and 1.13 mA cm⁻², respectively, which are also much higher than that of the Pt/C (0.35 mA cm⁻²). Collectively, the Rh@Pt_{3.5L} NW/C shows the best performance in both the mass activity and specific activity, which are 3.7 and 3.4 times those of the commercial Pt/C catalyst, respectively.

In order to evaluate the catalytic activities and the possible poisoning of the Rh@Pt_{nL} NW/C catalysts under continuous operation condition, we conducted chronoamperometric tests (*i*-*t*) for the electrocatalysts at 0.64 V (vs saturated calomel electrode (SCE)) and room temperature for 60 min. As shown in Figure 4c, there was a sharp decline in current during the initial several seconds, which has been ascribed to the adsorption of intermediates formed at the beginning of the oxidation reaction.^[47] As the reaction proceeded, the current gradually reached a more stable state due to the intermediates adsorbing and oxidizing rate approached a balance. It can be found that, in comparison with Pt/C, all the Rh@Pt_{nL} NW/C showed a much better capacity to overcome catalytic poisoning and, hence, exhibited a continuous higher current density in duration measurements. In addition, Rh is highly resistant to chemical corrosion and capable to stabilize the neighboring Pt atoms, which can also enhance the catalytic durability in acidic mediums.^[48–50]

The current peak for the back scanning (*I*_b) indicates the removal of the carbonaceous intermediates adsorbed on the catalysts. The relative intensity of *I*_{f1}/*I*_b has been widely adopted as an indicator for the amount of carbonaceous intermedium accumulated on the catalyst surfaces due to the incomplete

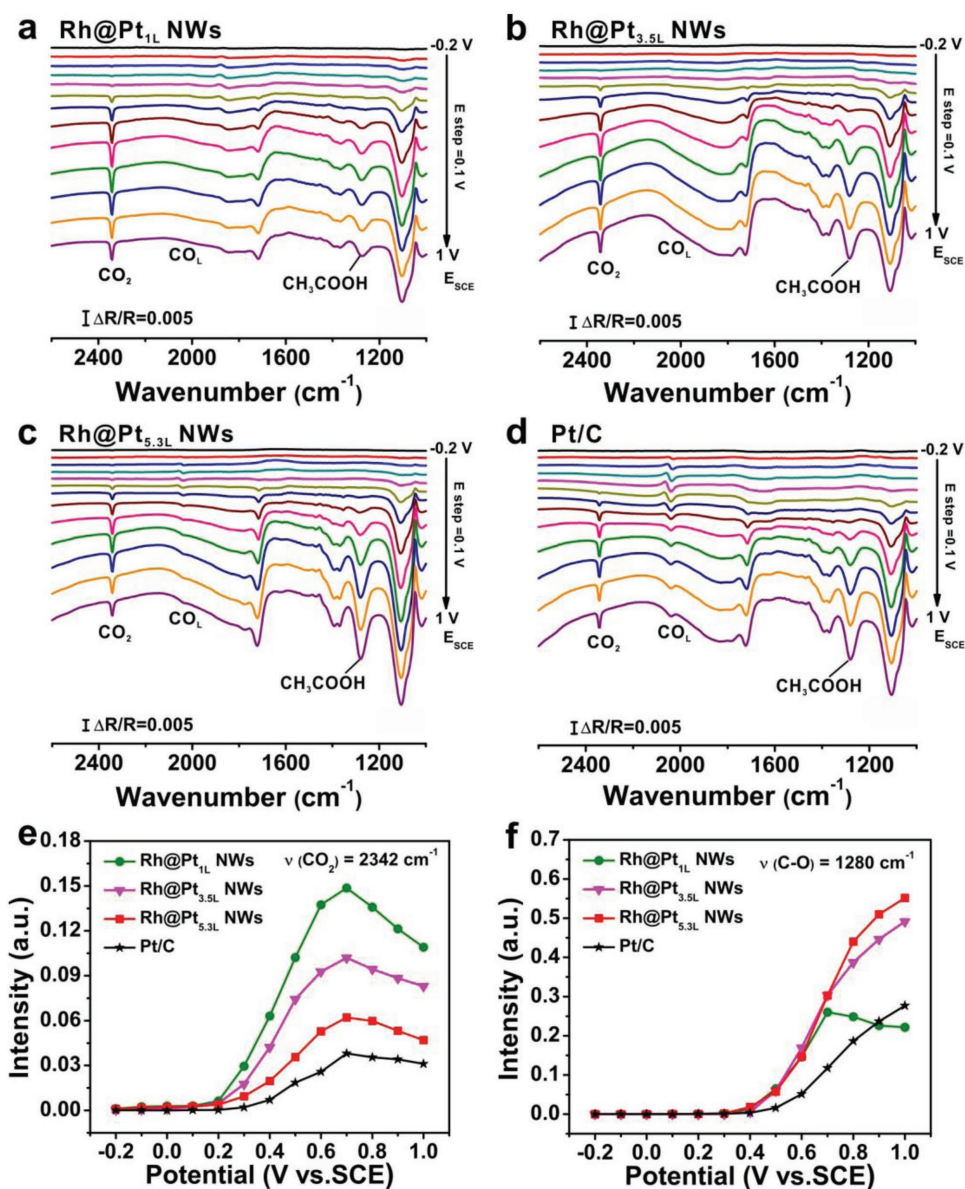


Figure 5. a–d) In situ FTIR spectra of the electrocatalysts for EOR in 0.2 M ethanol and 0.1 M HClO₄ solution: Rh@Pt_{1L} NW/C, Rh@Pt_{3.5L} NW/C, Rh@Pt_{5.3L} NW/C, and commercial Pt/C. e, f) Integrated in situ FTIR band intensities (normalized by Pt mass) of CO₂ (2342 cm⁻¹) and CH₃COOH (1280 cm⁻¹) from the compared electrocatalysts.

oxidation.^[51] In addition, the value of I_{f1}/I_{f2} signifies the capacity for the C–C bond cleavage of ethanol.^[39] As shown in Figure 4d and Table S3 (Supporting Information), both the values of I_{f1}/I_b and I_{f1}/I_{f2} on these Rh@Pt_{nL} NW/C derived from the EOR CV curves are obviously higher than that of the Pt/C, indicating the surface poisoning was inhibited and the cleavage of the C–C bond was promoted on these Rh@Pt_{nL} NWs/C catalysts. In particular, Rh@Pt_{1L} NW/C shows the maximum values of both I_{f1}/I_b (2.46) and I_{f1}/I_{f2} (1.12), which are 3.2 and 1.6 times that of the commercial Pt/C, respectively. Interestingly, these values were gradually decreased as the atomic layer numbers of the Pt shells increased, implying the closer interaction between the outermost Pt layers and the Rh substrates is more effective in mitigating the surface poisoning

and promoting the cleavage of the C–C bond of ethanol. This Pt atomic layer number dependent EOR behavior can be attributed to the variation of the geometric compression strain and the electronic ligand effects balanced by the Pt thickness.^[52]

In order to get deeper insights into the apparent activity and the product selectivity during EOR at molecular level, electrochemical in situ FTIR studies were carried out on these Rh@Pt_{nL} NW/C catalysts with altered Pt shell thicknesses. Figure 5a–d shows the in situ FTIR spectra on Rh@Pt_{1L} NW/C, Rh@Pt_{3.5L} NW/C, Rh@Pt_{5.3L} NW/C, and Pt/C catalysts during EOR. A number of absorption bands appeared with the increase of electrode potential (Table S4, Supporting Information). According to previous studies,^[53–56] the band at 2342 cm⁻¹ was attributed to the asymmetric stretch vibration of CO₂,

which reflects the cleavage of the C–C bond associated with the complete oxidation of ethanol. The bipolar band at round 2050 cm^{-1} was ascribed to the linearly adsorbed CO (CO_L), implying the CO adsorption on catalyst surfaces. The peak located around 1718 cm^{-1} was assigned to the stretching vibration of C=O bond in both acetaldehyde and acetic acid. Another band at 1280 cm^{-1} belongs to the C–O stretching deformation in CH_3COOH , which can be applied to monitor the production of CH_3COOH .

The evolution of the band integrated intensities normalized to the Pt mass as a function of electrode potential is shown in Figure S13 (Supporting Information). It can be observed that the $\text{Rh}@Pt_{nL}$ NW/C catalysts' selectivities toward CO_2 and CH_3COOH are very sensitive to the atomic layer number of the Pt shells, and are obviously improved compared to the commercial Pt/C. Particularly, the $\text{Rh}@Pt_{1L}$ NW/C shows the highest CO_2 selectivity but poorer CH_3COOH selectivity at the investigated potential windows (Figure 5e,f). With the increase of the outer Pt atomic layer numbers, the selectivity toward CO_2 was gradually decreased while the CH_3COOH selectivity was increased inversely. Also, the onset potential for generating CO_2 was lower on the catalysts with less Pt atomic layer numbers. In Rh–Pt bimetallic heterosystems, the strain and ligand effects from the Rh subsurface is a key factor for weakening Pt–intermediate binding strength (such as Pt–CO) to ease their oxidation.^[41] As the in situ FTIR spectra shown, no obvious CO_L band can be observed on the $\text{Rh}@Pt_{1L}$ NW/C and $\text{Rh}@Pt_{3.5L}$ NW/C catalysts, while a tiny CO_L signal and a larger one can be found on the $\text{Rh}@Pt_{5.3L}$ NW/C and the Pt/C, respectively. This result is well consistent with the chronoamperometric tests and the aforementioned $I_{\text{f}}/I_{\text{b}}$ values, indicating an improved anti CO-poisoning ability. Also, it has been demonstrated that the dehydrogenation process is favored on Pt sites, while C–C bond cleavage prefers Rh sites.^[56] The less atomic layer number of the Pt shell causes stronger Rh–Pt interaction compression strain and larger electronic ligand effect on the outermost Pt surface, which can dramatically alter the catalytic behavior of the outermost Pt surface leading to the priority of C–C bond cleavage. When the Pt shell thickened, the strain effects and ligand effects were gradually released, and the catalytic properties of outermost Pt shell tended to be the nature of pristine Pt, as the geometric strain and ligand effect can only impact surface reactivity over less than a few atomic layers.^[20,24] Thus, the $\text{Rh}@Pt_{5.3L}$ NW/C catalysts presented the highest capacity for producing acetic acid but poor selectivity toward CO_2 . It has been demonstrated that the CO_2 current efficiency (a quantification of the current generated from the CO_2 pathway reported to the EOR overall current) is generally found to be only between 5 and 20%.^[57] The overall activity for EOR should integrate both the CO_2 and $\text{CH}_3\text{CH}_2\text{OH}$ pathways into account. As a result, the $\text{Rh}@Pt_{3.5L}$ NW/C catalysts possess the greatest mass activity and specific activity in the scope of this study.

3. Conclusion

In summary, this work demonstrates the successful synthesis of ultrathin $\text{Rh}@Pt_{nL}$ core–sheath NWs with controlled Pt atomic layer number and faithful replication of the high-density

GBs of the Rh NW cores on the outermost Pt shells. When loaded on carbon support, the $\text{Rh}@Pt_{nL}$ NW catalysts show greatly improved behaviors for catalyzing EOR in both activity and durability. As the balance of compression strain and ligand effects between the Rh nanowires and the Pt shells, the EOR performances are highly dependent on the number of the outer Pt atomic layers. Electrochemical in situ FTIR spectroscopy indicated that thinner Pt shell (i.e., $\text{Rh}@Pt_{1L}$ NW/C catalysts) has better capacity to break the C–C bond for complete oxidation of ethanol to CO_2 but poorer ability for dehydrogenation of ethanol to acetic acid. With the increase of the Pt shell thickness, the CO_2 pathway is weakened down and the formation of acetic acid is boosted up on the core–sheath catalysts. Overall, the $\text{Rh}@Pt_{3.5L}$ NWs show the best performance in both the mass activity and specific activity.

4. Experimental Section

Chemicals: Sodium hexachlororhodate (III) dodecahydrate ($\text{Na}_3\text{RhCl}_6\cdot 12\text{H}_2\text{O}$) was purchased from Alfa Aesar. Chloroplatinic acid hexahydrate ($\text{H}_2\text{PtCl}_6\cdot 6\text{H}_2\text{O}$, Pt $\geq 37.5\%$) and perchloric acid (HClO_4 , 70%) were purchased from Aladdin. Polyvinylpyrrolidone (PVP, MW $\approx 55\ 000$) was purchased from Sigma-Aldrich. Sodium iodide dihydrate ($\text{NaI}\cdot 2\text{H}_2\text{O}$, $\geq 99.0\%$) and ethanol ($\text{C}_2\text{H}_5\text{OH}$, $\geq 99.7\%$) were purchased from Xilong Chemical Co. Ltd. Sodium ascorbate (NaAA), acetone ($\text{C}_3\text{H}_6\text{O}$, $\geq 99.5\%$), and ethylene glycol (EG, $\geq 99.0\%$) were purchased from Sinopharm Chemical Reagent Co. Ltd. Ultrapure water (18.2 M Ω) was used in all experiments. All reagents were used as received, without further purification.

Synthesis of 1.9 nm Rh Wavy Nanowires: In a typical synthesis of the 1.9 nm Rh wavy nanowires, $\text{Na}_3\text{RhCl}_6\cdot 12\text{H}_2\text{O}$ (15.6 mg, 0.026 mmol), $\text{NaI}\cdot 2\text{H}_2\text{O}$ (93 mg, 0.5 mmol), NaAA (40 mg, 0.2 mmol), and PVP (160 mg) were mixed together with EG (5.0 mL) and H_2O (1.0 mL) in a 25 mL glass vial. After the vial was capped, the mixture was ultrasonicated for around 6 min and then magnetically stirred at 360 rpm for 10 min. The obtained mixture was heated at $170\text{ }^\circ\text{C}$ in an oil bath under magnetic stirring for 2 h. The products were cooled down to room temperature and washed with ethanol/acetone four times, collected by centrifugation and then redispersed in 10 mL EG.

Synthesis of $\text{Rh}@Pt_{nL}$ Core–Sheath Nanowires: Typically, 2.0 mL EG solution of the as-prepared Rh nanowires and 5.0 mL EG were added together in a 25 mL glass vial. The mixture (Solution A) was ultrasonicated for 7 min and then magnetically stirred at room temperature for another 7 min to make sure the Rh NWs were well dispersed. Solution A was then preheated in an oil bath at $120\text{ }^\circ\text{C}$ for 10 min under magnetic stirring (360 rpm). The Pt precursor solution (Solution B) was prepared by dissolving quantitative $\text{H}_2\text{PtCl}_6\cdot 6\text{H}_2\text{O}$ (2.2 mg mL^{-1}) and PVP (83 mg mL^{-1}) together in EG. To obtain $\text{Rh}@Pt_{1L}$ NWs, $\text{Rh}@Pt_{2L}$ NWs, $\text{Rh}@Pt_{3.5L}$ NWs, and $\text{Rh}@Pt_{5.3L}$ NWs, a series of volumes of solution B, that is, 0.3, 0.6, 1.2, and 2.4 mL, were added into the preheated Solution A, respectively. The total volumes of the reaction solutions were all set to 10 mL by extra additions of EG. The reaction solution was maintained at $120\text{ }^\circ\text{C}$ in the oil bath with magnetic stirring for 4 h. The final products were cooled down to room temperature, collected by centrifugation (14 000 rpm, 10 min) and washed four times with a mixture of ethanol and acetone.

Characterizations: XRD analysis was performed using a Rigaku Smar/SmartLa operating at 30 mA and 40 kV using a Cu $K\alpha$ radiation ($\lambda = 1.541\text{ \AA}$), in a range of 2θ from 30° to 90° at a scan rate of 5° min^{-1} . TEM images, EDS elemental mappings, and cross-sectional compositional line scanning profiles were conducted with a Hitachi H-7650 operated at 100 kV, an FEI Tecnai G2 F30 S-Twin at 300 kV, and a JEOL ARM200 microscope with a STEM Cs corrector. The EDS elemental analysis was also recorded on a Hitachi S4800 equipped with

an energy-dispersive X-ray spectrometer. The elemental contents of Rh and Pt were analyzed by an Agilent 7800 ICP-MS. XPS analysis was performed on a ThermoFisher ESCALAB250. The XPS spectra were all corrected by C 1s peak (284.6 eV).

Electrocatalysis Measurements: Before the electrocatalytic tests, the Rh@Pt_{nL} NWs were loaded on Vulcan XC-72 carbon (25 wt% of total metals, determined by ICP-MS). Typically, 9.0 mg Vulcan XC-72 carbon was dispersed in 9.0 mL ethanol and then ultrasonicated for 1 h. After that, the dispersion of Rh@Pt_{nL} NWs in ethanol (containing 3.0 mg of total metals, determined by ICP-MS) was dropwise added into the homogeneous carbon solution under vigorously magnetic stirring. The obtained solution was further ultrasonicated for 1 h and magnetically stirred for 3 h. The loaded Rh@Pt_{nL} NW/C electrocatalysts were collected by centrifugation and redispersed in 10 mL acetic acid, heated at 60 °C for 12 h with magnetic stirring to clean the surface of the Rh@Pt_{nL} NWs. The cleaned catalysts were washed thrice with ethanol, dried under vacuum condition, and then annealed at 200 °C for 1 h. The electrocatalyst inks were prepared by redispersing the Rh@Pt_{nL} NW/C (4.8 mg) or the commercial Pt/C (6 mg, 20 wt%, JM) catalysts in 2 mL mixed solution of ethanol and 5% Nafion (vol:vol = 1:0.005), respectively. 5 μL of the ink was dropped on a glassy-carbon electrode (GCE, diameter: 5 mm, area: 0.196 cm², Tianjin Aida Co., China) and then dried in room temperature naturally. Therefore, the loading concentration of metal nanocatalysts for Rh@Pt_{nL} NW/C and commercial Pt/C was 15.3 μg_{Rh+Pt} cm⁻² and 15.3 μg_{Pt} cm⁻², respectively, according to the geometric electrode area.

All electrochemical measurements were conducted on a CHI 760E electrochemical workstation (Shanghai Chenhua Co., China). A three-electrode system was used to conduct the electrochemical measurements. The SCE was used as reference electrode, a Pt mesh (1 × 1 cm²) was served as counter electrodes, and a catalyst-loaded GCE (diameter: 5 mm) was served as working electrode. The ECSAs were determined by integrating the hydrogen desorption/adsorption charge on the cyclic voltammograms (CVs) recorded between -0.25 and 0.95 V (vs SCE) at a sweep rate of 50 mV s⁻¹ in N₂-saturated 0.1 M HClO₄ solution. Electrocatalytic oxidation of ethanol was recorded between -0.25 and 1.20 V (vs SCE) at a sweep rate of 50 mV s⁻¹ in N₂-saturated 0.1 M HClO₄ and 0.2 M ethanol solution.

Electrochemical In Situ FTIR Studies for Ethanol Oxidation: In order to study the product selectivity and reaction mechanisms of ethanol oxidation reaction for different catalysts, in situ FTIR spectroscopic studies were carried out on a Nexus 870 FTIR spectrometer (Nicolet) fitted out a MCT detector cooled with liquid nitrogen and an EverGlo IR source. In this configuration, infrared radiation sequentially passed through a CaF₂ window and a thin-layer solution (≈10 μm), and then it was reflected by the electrode surface, at a spectral resolution of 8 cm⁻¹. The resulting spectra were reported as relative change in reflectivity

$$\frac{\Delta R}{R} = \frac{R(E_S) - R(E_R)}{R(E_R)} \quad (1)$$

where $R(E_S)$ and $R(E_R)$ are the single-beam spectra collected at sample potential E_S and reference potential E_R , respectively. The E_R was recorded at -0.25 V (vs SCE).

Supporting Information

Supporting Information is available from the Wiley Online Library or from the author.

Acknowledgements

This work was supported by the National Natural Science Foundation of China (21771067), the Natural Science Foundation of Fujian Province (Distinguished Young Investigator, 2017J06005), the Natural Science

Foundation of Guangdong Province (2015A030310011), and the Scientific Research Funds and Subsidized Project for Postgraduates' Innovative Fund in Scientific Research of Huaqiao University. The authors thank Dr. Lu Lu from the Jia-Lab for Interface and Atomic Structure of Xi'an Jiaotong University for Cs-corrected STEM characterizations. The authors also thank the Instrumental Analysis Center of Huaqiao University for analysis support.

Conflict of Interest

The authors declare no conflict of interest.

Keywords

C–C bond cleavage, core–sheath nanowire, ethanol oxidation, grain boundary, PtRh bimetallic

Received: September 5, 2018

Revised: October 22, 2018

Published online:

- [1] F. T. Wagner, B. Lakshmanan, M. F. Mathias, *J. Phys. Chem. Lett.* **2010**, *1*, 2204.
- [2] M. K. Debe, *Nature* **2012**, *486*, 43.
- [3] P. Strasser, *Science* **2015**, *349*, 379.
- [4] M. Shao, Q. Chang, J.-P. Dodelet, R. Chenitz, *Chem. Rev.* **2016**, *116*, 3594.
- [5] Z. W. Seh, J. Kibsgaard, C. F. Dickens, I. Chorkendorff, J. K. Nørskov, T. F. Jaramillo, *Science* **2017**, *355*, eaad4998.
- [6] N. Tian, Z. Y. Zhou, S. G. Sun, Y. Ding, Z. L. Wang, *Science* **2007**, *316*, 732.
- [7] N. S. Porter, H. Wu, Z. Quan, J. Fang, *Acc. Chem. Res.* **2013**, *46*, 1867.
- [8] Y. J. Wang, W. Long, L. Wang, R. Yuan, A. Ignaszak, B. Fang, D. P. Wilkinson, *Energy Environ. Sci.* **2018**, *11*, 258.
- [9] Y. Sun, L. Zhuang, J. Lu, X. Hong, P. Liu, *J. Am. Chem. Soc.* **2007**, *129*, 15465.
- [10] A. Chen, P. Holt-Hindle, *Chem. Rev.* **2010**, *110*, 3767.
- [11] R. Lin, X. Cai, H. Zeng, Z. Yu, *Adv. Mater.* **2018**, *30*, 1705332.
- [12] D. Y. Chung, J. M. Yoo, Y.-E. Sung, *Adv. Mater.* **2018**, *30*, 1704123.
- [13] P. Rodriguez, Y. Kwon, M. T. M. Koper, *Nat. Chem.* **2012**, *4*, 177.
- [14] E. Antolini, *J. Power Sources* **2007**, *170*, 1.
- [15] H. F. Wang, Z. P. Liu, *J. Am. Chem. Soc.* **2008**, *130*, 10996.
- [16] A. Kowal, M. Li, M. Shao, K. Sasaki, M. B. Vukmirovic, J. Zhang, N. S. Marinkovic, P. Liu, A. I. Frenkel, R. R. Adzic, *Nat. Mater.* **2009**, *8*, 325.
- [17] W. Zhu, J. Ke, S. B. Wang, J. Ren, H. H. Wang, Z. Y. Zhou, R. Si, Y. W. Zhang, C. H. Yan, *ACS Catal.* **2015**, *5*, 1995.
- [18] J. Gu, Y. W. Zhang, F. Tao, *Chem. Soc. Rev.* **2012**, *41*, 8050.
- [19] Y. Xiong, H. Shan, Z. Zhou, Y. Yan, W. Chen, Y. Yang, Y. Liu, H. Tian, J. Wu, H. Zhang, D. Yang, *Small* **2017**, *13*, 1603423.
- [20] K. D. Gilroy, X. Yang, S. Xie, M. Zhao, D. Qin, Y. Xia, *Adv. Mater.* **2018**, *30*, 1706312.
- [21] S. Xie, S.-I. Choi, N. Lu, L. T. Roling, J. A. Herron, L. Zhang, J. Park, J. Wang, M. J. Kim, Z. Xie, M. Mavrikakis, Y. Xia, *Nano Lett.* **2014**, *14*, 3570.
- [22] Y. Wang, W. Wang, F. Xue, Y. Cheng, K. Liu, Q. Zhang, M. Liu, S. Xie, *Chem. Commun.* **2018**, *54*, 5185.
- [23] B. W. Zhang, H. L. Yang, Y. X. Wang, S. X. Dou, H. K. Liu, *Adv. Energy Mater.* **2018**, *8*, 1703597.
- [24] P. Strasser, S. Koh, T. Anniyev, J. Greeley, K. More, C. Yu, Z. Liu, S. Kaya, D. Nordlund, H. Ogasawara, M. F. Toney, A. Nilsson, *Nat. Chem.* **2010**, *2*, 454.

- [25] L. Bu, N. Zhang, S. Guo, X. Zhang, J. Li, J. Yao, T. Wu, G. Lu, J. Y. Ma, D. Su, X. Huang, *Science* **2016**, 354, 1410.
- [26] C. W. Li, J. Ciston, M. W. Kanan, *Nature* **2014**, 508, 504.
- [27] X. Huang, Z. Zhao, Y. Chen, C.-Y. Chiu, L. Ruan, Y. Liu, M. Li, X. Duan, Y. Huang, *Nano Lett.* **2014**, 14, 3887.
- [28] S.-I. Choi, J. A. Herron, J. Scaranto, H. Huang, Y. Wang, X. Xia, T. Lv, J. Park, H.-C. Peng, M. Mavrikakis, Y. Xia, *ChemCatChem* **2015**, 7, 2077.
- [29] S. Xie, Q. Xu, X. Huang, *ChemCatChem* **2016**, 8, 480.
- [30] H. G. Liao, L. Cui, S. Whitelam, H. Zheng, *Science* **2012**, 336, 1011.
- [31] Y. Wang, S.-I. Choi, X. Zhao, S. Xie, H.-C. Peng, M. Chi, C. Z. Huang, Y. Xia, *Adv. Funct. Mater.* **2014**, 24, 131.
- [32] R. Blume, H. Niehus, H. Conrad, A. Böttcher, *J. Phys. Chem. B* **2004**, 108, 14332.
- [33] Y. Yang, J. Zhang, Y. Wei, Q. Chen, Z. Cao, H. Li, J. Chen, J. Shi, Z. Xie, L. Zheng, *Nano Res.* **2018**, 11, 656.
- [34] X. Sun, K. Jiang, N. Zhang, S. Guo, X. Huang, *ACS Nano* **2015**, 9, 7634.
- [35] M. Wakisaka, S. Mitsui, Y. Hirose, K. Kawashima, H. Uchida, M. Watanabe, *J. Phys. Chem. B* **2006**, 110, 23489.
- [36] J.-X. Tang, Q.-S. Chen, L.-X. You, H.-G. Liao, S.-G. Sun, S.-G. Zhou, Z.-N. Xu, Y.-M. Chen, G.-C. Guo, *J. Mater. Chem. A* **2018**, 6, 2327.
- [37] E. W. Harak, K. M. Koczur, D. W. Harak, P. Patton, S. E. Skrabalak, *ChemNanoMat* **2017**, 3, 779.
- [38] J. P. I. de Souza, S. L. Queiroz, K. Bergamaski, E. R. Gonzalez, F. C. Nart, *J. Phys. Chem. B* **2002**, 106, 9825.
- [39] L. Rao, Y. X. Jiang, B. W. Zhang, Y. R. Cai, S. G. Sun, *Phys. Chem. Chem. Phys.* **2014**, 16, 13662.
- [40] J. Bai, X. Xiao, Y. Y. Xue, J. X. Jiang, J. H. Zeng, X. F. Li, Y. Chen, *ACS Appl. Mater. Interfaces* **2018**, 10, 19755.
- [41] V. D. Colle, V. Grozovski, E. Herrero, J. M. Feliu, *ChemCatChem* **2013**, 5, 1350.
- [42] Z. Y. Zhou, Z. Z. Huang, D. J. Chen, Q. Wang, N. Tian, S. G. Sun, *Angew. Chem., Int. Ed.* **2010**, 49, 411.
- [43] Z.-B. Wang, G.-P. Yin, J. Zhang, Y.-C. Sun, P.-F. Shi, *J. Power Sources* **2006**, 160, 37.
- [44] X. Huang, Z. Zhao, J. Fan, Y. Tan, N. Zheng, *J. Am. Chem. Soc.* **2011**, 133, 4718.
- [45] Y. Shen, Z. Zhang, K. Xiao, J. Xi, *ChemCatChem* **2014**, 6, 3254.
- [46] J. Ding, L. Bu, S. Guo, Z. Zhao, E. Zhu, Y. Huang, X. Huang, *Nano Lett.* **2016**, 16, 2762.
- [47] J. E. Sulaiman, S. Zhu, Z. Xing, Q. Chang, M. Shao, *ACS Catal.* **2017**, 7, 5134.
- [48] S. Xie, N. Lu, Z. Xie, J. Wang, M. J. Kim, Y. Xia, *Angew. Chem., Int. Ed.* **2012**, 51, 10266.
- [49] V. Beermann, M. Gocyla, E. Willinger, S. Rudi, M. Heggen, R. E. Dunin-Borkowski, M.-G. Willinger, P. Strasser, *Nano Lett.* **2016**, 16, 1719.
- [50] H. Huang, K. Li, Z. Chen, L. Luo, Y. Gu, D. Zhang, C. Ma, R. Si, J. Yang, Z. Peng, J. Zeng, *J. Am. Chem. Soc.* **2017**, 139, 8152.
- [51] Z. Liu, X. Y. Ling, X. Su, J. Y. Lee, L. M. Gan, *J. Power Sources* **2005**, 149, 1.
- [52] D. Friebel, V. Viswanathan, D. J. Miller, T. Anniyev, H. Ogasawara, A. H. Larsen, C. P. O'Grady, J. K. Nørskov, A. Nilsson, *J. Am. Chem. Soc.* **2012**, 134, 9664.
- [53] N. Erini, R. Loukrakpam, V. Petkov, E. A. Baranova, R. Yang, D. Teschner, Y. Huang, S. R. Brankovic, P. Strasser, *ACS Catal.* **2014**, 4, 1859.
- [54] M. Heinen, Z. Jusys, R. J. Behm, *J. Phys. Chem. C* **2010**, 114, 9850.
- [55] E. A. de Souza, M. J. Giz, G. A. Camara, E. Antolini, R. R. Passos, *Electrochim. Acta* **2014**, 147, 483.
- [56] N. Erini, V. Beermann, M. Gocyla, M. Gliech, M. Heggen, R. E. Dunin-Borkowski, P. Strasser, *Angew. Chem., Int. Ed.* **2017**, 56, 6533.
- [57] A. B. Delpuech, M. Chatenet, M. S. Rau, C. Cremers, *Phys. Chem. Chem. Phys.* **2015**, 17, 10881.